Investigating 1st and 2nd order Fermi acceleration of energetic particles by small-scale magnetic flux ropes at 1AU

Journal of Physics: Conference Series **1620** (2020) 012008 doi:10.1088/1742-6596/1620/1/012008

Investigating 1st and 2nd order Fermi acceleration of energetic particles by small-scale magnetic flux ropes at 1AU

J A le Roux[1,2], G M Webb[2], O V Khabarova[3], K T Van Eck[2], L-L Zhao[2], L Adhikari[2]

[1] Department of Space Science, University of Alabama in Huntsville (UAH), 320 Sparkman Drive, AL 35805, USA
[2]Center of Space Plasma Science and Aeronomic Research (CSPAR), University of Alabama in Huntsville (UAH), 320 Sparkman Drive, AL 35805, USA
[3]Heliophysics Laboratory, Pushkov Institute for Terrestrial Magnetism, Ionosphere, and Radio Wave Propagation (IZMIRAN), Moscow, 108840, Russia

jar0013@uah.edu

Abstract. A new telegrapher-type Parker transport equation was derived from the existing underlying focused transport equation to model the acceleration of energetic particles by contracting and reconnecting small-scale magnetic flux ropes (SMFRs) in the large-scale solar wind. Time-dependent and steady-state analytical solutions were found that unify all SMFR acceleration mechanisms present in the transport equation, showing that SMFR acceleration by the parallel reconnection electric field in the mixed spatial and momentum derivative transport term is constrained by and requires the presence of 2nd order Fermi SMFR acceleration. We explore the potential of these solutions in reproducing energetic proton flux enhancements and spectral evolution between ~50 keV-5 MeV in dynamic SMFR regions near large-scale reconnecting current sheets in the solar wind at 1 AU. It is shown that both 2nd order Fermi SMFR acceleration involving the variance in SMFR compression and incompressible parallel shear flow, and 1st order SMFR Fermi acceleration due to mean SMFR compression are both workable options in reproducing observed flux amplification factors when using reasonable SMFR parameters. However, the predicted substantial quantitative differences in the spatial evolution of the accelerated spectra through the SMFR region might provide a diagnostic to distinguish between 1st and 2nd order Fermi SMFR acceleration in observations.

1. Motivation

Analytical one-dimensional (1D) steady-state solutions of diffusive Parker transport equations for small-scale magnetic flux rope (SMFR) acceleration of energetic ions showed promise in reproducing qualitatively the observed features of energetic ion acceleration in SMFR regions in the solar wind [1, 2, 3, 4]. The main features of SMFR acceleration identified in observations are: (1) Energetic particle fluxes increase in regions of dynamic SMFRs in the vicinity of magnetically reconnecting large-scale current sheets in such a way that the maximum flux amplification factor is larger for higher energy particles. In the inner heliosphere such increases were observed for ions up to 5 MeV and for electrons up to ~100 keV (See Figure 1, [9], and [12]). (2) Often the accelerated spectra are observed to harden going through the SMFR region adjacent to large-scale current sheets [5, 6].

Recently Zhao et al. [5], and Adhikari et al. [6] went a step further by reproducing remarkably well these acceleration features for observations of energetic ions in SMFR regions at 5 AU and 1 AU, respectively. This was accomplished by considering two SMFR acceleration mechanisms, namely, 1st order Fermi acceleration involving the mean SMFR compression rate and acceleration by the average parallel reconnection electric field generated at secondary (small-scale) reconnecting current sheets in merging SMFRs. The latter mechanism appears as a mixed spatial and momentum derivative term in the Parker transport equation [1, 2]. The same model also reproduced anomalous cosmic ray (ACR) features behind the heliospheric termination shock successfully [7]. In this model the 1st order Fermi SMFR acceleration was specified to be the dominant process, because otherwise it would not have been possible to generate accelerated particle flux enhancements downstream of the shock [1]. An important element in the success of this approach was the addition of a loss term to model the effect of particle escape from the SMFR region. This ensured steeper accelerated particle spectra closer to the observed spectral slopes. This modeling approach, however, did not address the role of 2nd order Fermi acceleration by SMFRs, and specified propagation and acceleration time scales without making a connection to SMFR parameters.

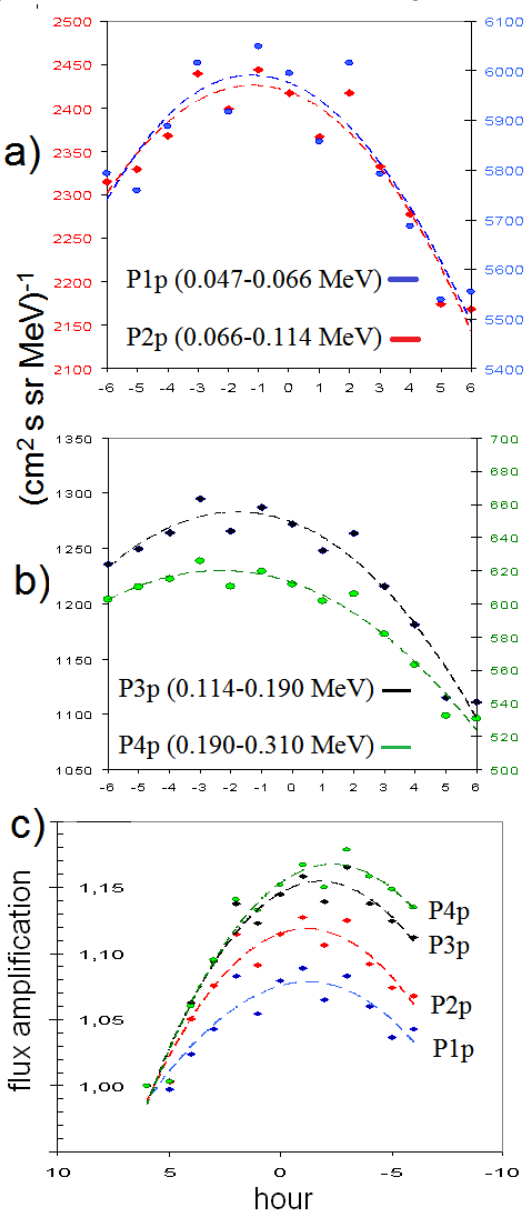

Figure 1. The characteristic observed features of energetic ion fluxes at and in the vicinity of SMFRs based on a statistical analysis of 11,372 SMFRs from 2005-2009 (the declining phase and minimum solar activity cycle) recorded in the data base at http://fluxrope.info/ [13]. (a) and (b) SMFR events are compared with the ACE EPAM LEMS120 (Low Energy Magnetic Spectrometer) energetic ion flux hourly data in four energy channels ranging from 0.047 to 0.31 MeV, The fluxes are averaged around the center of each SMFR (0 hour) using a superposed epoch analysis method. (c) The average flux amplification factor is calculated on the basis of (a) and (b) by normalizing ion flux at each point to the corresponding flux level at the right boundary where the amplification factor is 1 (no amplification). The maximum amplification factor for higher energy channels are larger and shifted further downstream of the normalization boundary, in qualitative agreement with the predicted signature of particle acceleration associated with dynamic SMFRs as shown in [1-4]. The average amplification factors are of modest size due to the large number of SMFR events considered. Observed amplification factors may be significantly larger for a more targeted set of SMFR events (see below).

To address these outstanding issues, we derived a new telegrapher Parker transport equation from the underlying SMFR focused transport equation and present the first time-dependent analytical solutions for energetic particle SMFR acceleration [8]. The solution for the first time unify all the SMFR acceleration mechanisms present in the focused transport equation (compression and parallel

shear flow acceleration, acceleration by the non-inertial force associated with the acceleration of the SMFR flow, and acceleration by the parallel electric field force [11]), enabling us to model 1st order Fermi SMFR compression acceleration and acceleration by the SMFR parallel reconnection electric field due to the mixed derivative transport term, as was done previously [5, 6, 7], but also 2nd order Fermi SMFR acceleration. We explore the possibility of reproducing 1 AU observations of accelerated energetic ion flux enhancements and the spatial evolution of the accelerated particle spectra in active SMFR regions [6, 9] for both 1st and 2nd order Fermi SMFR acceleration when restricting ourselves to reasonable SMFR parameters. Also considered is the question of whether one can develop a diagnostic for distinguishing between 1st and 2nd order Fermi SMFR acceleration in observations.

2. The telegrapher Parker transport equation

In [8] we present the complete telegrapher Parker transport equation that we derived from the underlying focused transport for SMFR acceleration. This was accomplished by expanding the energetic particle distribution up to the 2nd anisotropic moment with respect to particle pitch angle using the standard technique of Legendre polynomials [1] and by taking moments of the focused transport equation with a certain approach to closure. Thus, the equation is only valid for nearly-isotropic energetic particle distributions in pitch-angle space due to the assumption of frequent pitch-angle scattering occurring on large spatial scales in the solar wind. More details can be found in [8]. We present a simplified one dimensional (1D) version of the complete telegrapher Parker transport equation that we were able to solve analytically. The equation, which models evolution of the direction-averaged particle distribution function $f(x,p,t)$ as a function of position x, momentum p, and time t, reads

$$\tau_{sc}^{I}\frac{\partial^2 f}{\partial t^2}+\frac{\partial f}{\partial t}+U_0^I\frac{\partial f}{\partial x}+\frac{1}{3}\langle v_{COM}^{I}\rangle p\frac{\partial f}{\partial p}$$
$$=\kappa_0^I\frac{\partial^2 f}{\partial x^2}+\frac{1}{p^2}\frac{\partial}{\partial p}\left(p^4 D_0^I\frac{\partial f}{\partial p}\right)+\frac{2}{3}U_E^I\cos\psi\frac{\partial}{\partial x}\left(p\frac{\partial f}{\partial p}\right)-\frac{f}{\tau_{esc}}+Q \quad (1)$$

where τ_{sc}^{I} is the particle scattering time and U_0^I is the effective advection velocity energetic particles experience in the x-direction with the expression $U_0^I=U_0-U_E^I\cos\psi$. In this expression U_0 is the average velocity of the solar wind specified to flow in the x-direction modified by U_E^I which represents the average advection velocity of particles in the magnetic guide/background field direction because of the mean parallel electric field generated in merging SMFRs. U_E^I is projected in the x-direction by the factor $\cos\psi$ (ψ is the angle between guide/background magnetic field and the solar wind flow direction). Furthermore, $\langle v_{COM}^{I}\rangle$ denotes the average compression rate of the SMFR region, while κ_0^I is the energetic particle parallel spatial diffusion coefficient projected in the x-direction according to the expression $\kappa_0^I=\kappa_{||}^I(\cos\psi)^2$ (parallel diffusion is assumed to occur when energetic particles undergo pitch-angle scattering in response to random mirroring forces in SMFRs [2, 11]. Also, D_0^I represents the relative 2nd order Fermi SMFR acceleration rate of energetic particles, τ_{esc} is the characteristic time scale on which energetic particles escape from the SMFR region[5,6], and Q is the particle source.

It should be noted that D_0^I is complicated because its expression combines two classes of 2nd order Fermi acceleration. The first is connected to energetic particles undergoing frequent pitch-angle scattering in the average electric fields generated in a dynamic multi-SMFR region whereas the second refers to particle response to statistical fluctuations in these electric fields [2, 11]. The assumption of a significant stochastic element in SMFR electric fields is supported by recent magnetic reconnection simulations [10]. In each class of 2nd order Fermi acceleration all of the four basic SMFR acceleration mechanisms in the underlying focused transport theory appear which are: (1) compression acceleration, parallel shear flow acceleration, acceleration by the non-inertial force associated with acceleration of the SMFR flow, and acceleration by the parallel reconnection electric field in merging

SMFRs. In this paper we will only focus on stochastic acceleration caused by the variance in the SMFR compression and parallel shear-flow rates because the analytical solution is limited to D_0^I being independent of particle speed. For more details, see [8].

3. Time-dependent solutions

3.1 Solution of telegrapher Parker transport equation

We specify a steady-state point source of energetic particles that are injected into the SMFR region at a constant rate dN_0/dt at position x_0 with a momentum p_0 according to the expression $Q = (dN_0/dt\,/4\pi p_0^2)\delta(x-x_0)\delta(p-p_0)$. Then the solution of equation (1) is

$$f(x,p,t) = \frac{1}{2\pi}\left(\frac{dN_0/dt}{4\pi p_0^3}\right)\frac{1}{\sqrt{\overline{D_0^I}\tau_{sc}^I}}e^{\frac{1}{2}\left[U_0^I+\frac{qU_E^I}{3}\right](x-x_0)}\left(\frac{p}{p_0}\right)^{-\frac{q}{2}}\int_0^t d\tau\, g(\tau) \tag{2}$$

where the integrand of the time integral is given by

$$g(\tau) = e^{-\left(\frac{1}{2}\frac{\tau}{\tau_{sc}^I}\right)}\frac{\cosh\left(c\sqrt{v_c^2\tau^2-d^2}\right)}{\sqrt{v_c^2\tau^2-d^2}} \tag{3}$$

and

$$\overline{D_0^I} = D_0^I\left(1-\frac{1}{9}\frac{(U_E^I)^2}{\kappa_0^I D_0^I}\right)$$

$$q = 3\left(1-\frac{1}{9}\frac{\langle v_{COM}^I\rangle - U_0^I U_E^I/\kappa_0^I}{D_0^I}\right)\Big/\left(1-\frac{1}{9}\frac{(U_E^I)^2}{\kappa_0^I D_0^I}\right)$$

$$c = \sqrt{\frac{\tau_{sc}^I}{\kappa_0^I}\left(\frac{1}{2\tau_{sc}^I}\right)^2-\left(\frac{U_0^I}{2\kappa_0^I}\right)^2-\frac{1}{\tau_{esc}\kappa_0^I}-\frac{\overline{D_0^I}}{\kappa_0^I}\left(\frac{q}{2}\right)^2}$$

$$d = \sqrt{(x-x_0)^2+\frac{\kappa_0^I}{\overline{D_0^I}}\left[\ln\left(\frac{p}{p_0}\right)-\frac{1}{3}\frac{U_E^I}{\kappa_0^I}(x-x_0)\right]^2} \tag{4}$$

Furthermore, $\tau = t' - t_0$ is the time interval relative to the initial time t_0, $v_c = v/\sqrt{3}$ is the speed of leading nearly isotropic energetic particle pulse (telegrapher speed). The solution is limited by the conditions $p \geq p_{0,}\, v_c\tau \geq d$ (causality condition), and $1-(U_E^I)^2/9\kappa_0^I D_0^I > 0$.

The causality condition can be further investigated by setting $v_c\tau - d = 0$ and solving for $\ln(p/p_0)$. This yields the expression

$$\ln\left(\frac{p}{p_0}\right) = \frac{1}{3}\frac{U_E^I}{\kappa_0^I}(x-x_0) \pm \frac{1}{\kappa_0^I}\sqrt{D_0^I\kappa_0^I\left(1-\frac{1}{9}\frac{(U_E^I)^2}{\kappa_0^I D_0^I}\right)[v_c^2\tau^2-(x-x_0)^2]} \tag{5}$$

For $\ln(p/p_0)$ to be real requires both $1-(U_E^I)^2/9\kappa_0^I D_0^I > 0$ and $v_c^2\tau^2-(x-x_0)^2 > 0$, or alternatively, that both $1-(U_E^I)^2/9\kappa_0^I D_0^I < 0$ and $v_c^2\tau^2-(x-x_0)^2 < 0$. In the latter case the second inequality implies that for any given time interval τ, particles do not reach the arbitrary observation position x so that the solution is $f(x,p,t) = 0$. This zero solution arises when $D_0^I < (U_E^I)^2/9\kappa_0^I$, that is, when 2nd order Fermi acceleration by SMFRs is less efficient compared to acceleration by the mean parallel reconnecting electric field in merging SMFRs through the mixed-derivative acceleration term (see equation (1)). In the framework of the telegrapher solution it is thus necessary to constrain the strength of particle acceleration by the mean parallel reconnection electric field of SMFRs sufficiently relative to 2nd order Fermi acceleration by SMFRs. Furthermore, a

solution of SMFR acceleration involving the mixed-derivative term is not viable without 2nd order Fermi acceleration, thus emphasizing the need for including the latter in SMFR acceleration studies. In other words, to study particle acceleration by the mean parallel reconnection electric field requires a complete description of the acceleration that includes both the mixed-derivative acceleration term and the 2nd order Fermi acceleration term associated with the parallel electric field. Note that this analytical solution and those further below are limited to constant transport coefficients.

3.2 Solution of time-dependent diffusive Parker transport equation

We also derived a time-dependent solution by neglecting the telegrapher term (1st term) in equation (1). The solution is similar to the telegrapher solution (equation (2)), and can be found by replacing the integrand of the time integral $g(\tau)$ in equation (2) with the new expression

$$g(\tau) = \sqrt{\frac{\tau_{sc}^I}{\kappa_0^I}}\frac{1}{2\tau}e^{-\frac{\alpha}{\tau}-\beta\tau} \tag{6}$$

where

$$\alpha = \frac{d^2}{4\kappa_0^I};\ \ \beta = \left(\frac{1}{2}\frac{U_0^I}{\kappa_0^I}\right)^2\kappa_0^I + \frac{1}{\tau_{esc}} + \left(\frac{q}{2}\right)^2\overline{D_0^I} \tag{7}$$

The expression for α is closely related to the expression for d in equation (4), while the expression for β is a simplified version of expression c in equation (4).

4. The steady-state solution

By letting the time interval $\tau \to \infty$ in integrand (6), one finds the steady-state solution of the time-dependent diffusive Parker transport equation which is

$$f(x,p,t) = \frac{1}{2\pi}\left(\frac{dN_0/dt}{4\pi p_0^3}\right)\frac{1}{\sqrt{\overline{D_0^I}\kappa_0^I}}e^{\frac{1}{2}\left[U_0^I+\frac{qU_E^I}{3}\right](x-x_0)}\left(\frac{p}{p_0}\right)^{-\frac{q}{2}}K_0(2\sqrt{\alpha\beta}) \tag{8}$$

where K_0 is the modified Bessel function of the 2nd kind. All the parameters in this solution have been defined above. Inspection of the solution reveals the basic characteristics of observations of energetic particle acceleration by and transport through a dynamic SMFR region in the solar wind, namely, energetic particle distribution spatial peak formation and spectral hardening [e.g., 5, 6]. By taking the limit $(\ln(p/p_0))^2 \gg (x-x_0)^2$ in the α-expression of the K_0 function in solution (8), the steady-state solution converges to

$$f(x,p) \propto e^{\frac{1u_0}{2\kappa_0^I}(x-x_0)}\left(\frac{p}{p_0}\right)^{-\frac{1}{2}\left[q+|q|\sqrt{1+\left(\frac{2}{q}\right)^2\tau_{D_0^I}\left(1/\tau_{\kappa_0^I}+1/\tau_{esc}\right)}\right]} \tag{9}$$

If the opposite limit $(ln(p/p_0))^2 \ll (x-x_0)^2$ is taken, the solution converges instead to

$$f(x,p) \propto e^{-\frac{1}{2}\left[|U_0(x-x_0)|\sqrt{1+4\tau_{\kappa_0^I}\left((q/2)^2/\tau_{D_0^I}+1/\tau_{esc}\right)}-U_0(x-x_0)\right]/\kappa_0^I}\left(\frac{p}{p_0}\right)^{-\frac{q}{2}} \tag{10}$$

In (9) and (10) we specified the characteristic time scales $\tau_{D_0^I} = 1/D_0^I$ (acceleration time scale for 2nd order Fermi acceleration), and $\tau_{\kappa_0^I} = \kappa_0^I/(U_0^I)^2$ (diffusion time scale). These solution limits were simplified for easier interpretation by putting $U_E^I = 0$, thus underplaying the effect of the mixed-derivative acceleration term which counteracts observed spatial peak formation in the accelerated particle distributions in SMFR regions [1]. Both solution limits (9) and (10) indicate that when energetic particle diffusive transport occurs against the solar wind flow upstream of the particle injection point ($x < x_0$), the particle distribution decays exponentially with increasing upstream distance relative to the particle point source (thus no spatial peak in the particle distribution).

Considering diffusive transport unfolding in the direction of the solar wind flow downstream of the injection point ($x > x_0$) during acceleration, the particle distribution increases exponentially with increasing distance downstream when sufficiently close to the particle source because then limit (9) applies. However, sufficiently far downstream of the injection point the particle distribution at lower energies decays first with increasing distance because then limit (10) is applicable. The decay at higher energies occurs progressively further downstream of the particle source when limit (10) becomes applicable at those distances. Thus, peaks form in the accelerated downstream distribution that shifts increasingly to larger distances downstream with increasing particle energy.

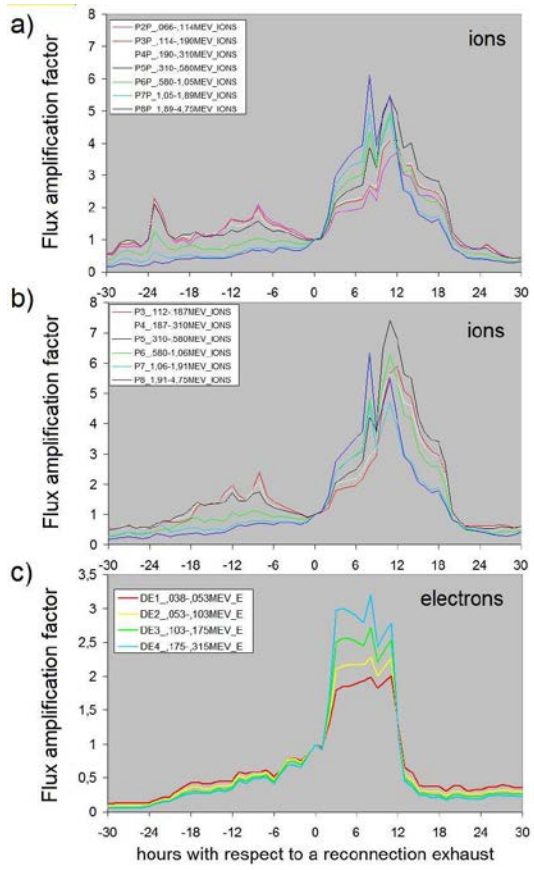

Figure 2. Variations of the averaged energetic particle flux amplification factor with respect to reconnection exhausts (large-scale current sheets) detected with the ACE spacecraft according to a superposed epoch analysis from Khabarova & Zank [9] involving 126 Petschek-type reconnection exhaust events. Zero hour corresponds to the occurrence of each reconnection exhaust. From the ACE Electron, Proton, and Alpha Monitor (EPAM) we display from top to bottom energetic ion flux from the LEMS120 telescope in (a) and the LEMS30 detector in (b), and energetic electron flux measurements from detector CA60 in (c).

Consider the accelerated particle spectra. Close to the particle source the particle spectra form power laws steeper than $f(p) \propto (p/p_0)^{-q/2}$ at most energies above the injection energy ($p > p_0$) because the spectrum converges to the limit given by (9). With increasing distance downstream of the injection position limit (9) applies progressively at increasingly high particle energies only while at lower energies limit (10) applies where the spectrum approaches the harder power law $f(p) \propto (p/p_0)^{-q/2}$ for a growing energy interval. Thus, with increasing distance downstream of the particle source the accelerated particle spectrum becomes increasingly hard while assuming a more exponential character as it bends over more strongly at lower energies [5]. Inspection of limit (9) also reveals that more efficient particle escape results in a steeper spectrum [5] and a larger spatial diffusion coefficient produces a harder spectrum as particles sample more SMFRs in a given time interval.

5. Modeling SMFR acceleration events near Earth orbit with the steady-state solution

5.1 2nd order Fermi acceleration by SMFRs

In Figure 3 we display steady-state solution (8) in the limit assuming 2nd order Fermi SMFR acceleration due the variance in the SMFR compression and parallel shear flow rates is the dominant acceleration mechanism. This was accomplished by specifying $\langle v_{COM}^I \rangle = 0$ and $U_E^I = 0$ in equation (8). The left panel in Figure 3 illustrates the spatial variation in the accelerated proton distribution function amplification factor for different particle energies downstream of the particle source ($x > x_0$) by choosing an amplification factor of one (no amplification) for all energies at the particle source position ($x = x_0$). The maximum amplification factor varies between ~2.8-5.4 for proton energies in the range 0.144-3.31 MeV, thus increasing with energy. This should be compared with Figure 2, and

with Figures 10 and 11 of [9] where, based epoch analysis of energetic ion flux enhancements in the vicinity of 126 thin primary reconnecting current sheet events at 1 AU, it was suggested that the

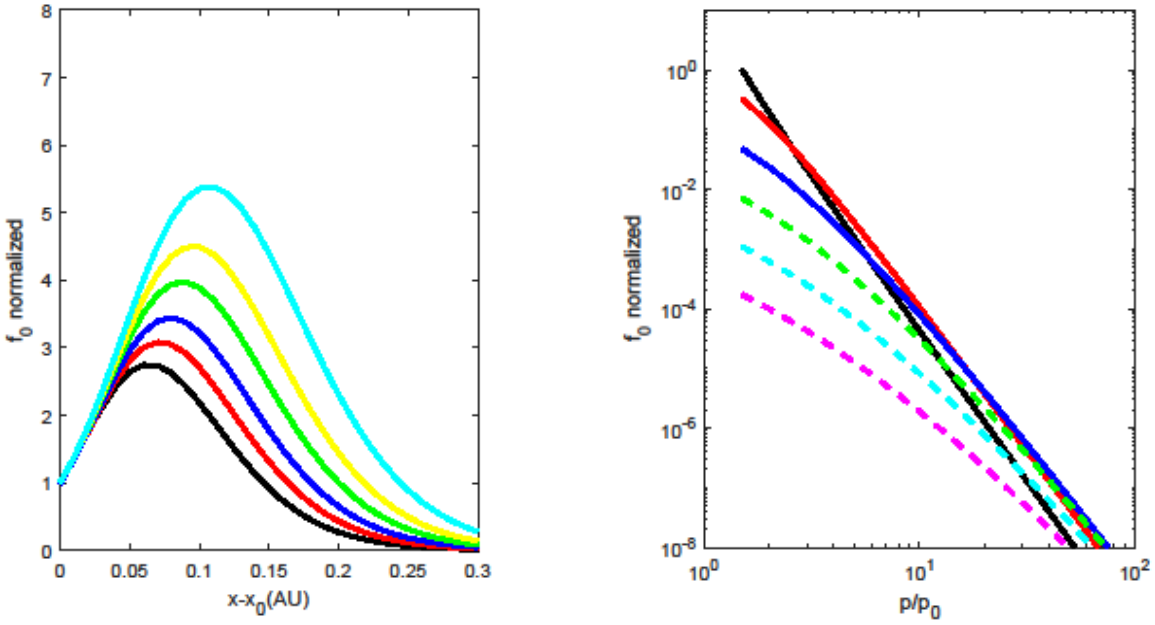

Figure 3. The 1D steady-state analytical solution for energetic proton 2nd order Fermi acceleration by SMFRs due the variance in the SMFR compression and parallel shear flow rate. Left panel: The direction-averaged proton distribution function $f(x,p)$ as a function of distance in AU downstream of the particle injection position $(x-x_0)$ for particle energies 144 keV (black), 256 keV (red), 0.44 MeV (blue), 0.81 MeV (green), 1.44 MeV (yellow), and 3.31 MeV (cyan). The energy intervals fall inside those in the observed energetic flux enhancements at 1 AU in Figure 1 [9]. The spatial curves were normalized to a value of 1 at the particle source $(x-x_0=0)$, thus revealing the amplification factor downstream. Right panel: Normalized $f(x,p)$ as a function particle momentum p in the solar wind frame normalized to p_0 (the injection momentum). The spectra are displayed for the following values of $x-x_0$: 0 AU (solid black), 0.05 AU (solid red), 0.1 AU (solid blue), 0.15 AU (dashed green), 0.2 AU (dashed cyan), and 0.25 AU (dashed magenta). The curves were multiplied with the same factor so that the black curve has a value of one at the minimum momentum $p/p_0=1.5$. At $p/p_0=1$ the proton kinetic energy $T\approx 1$ keV while at the maximum momentum $p/p_0=100, T\approx$ 10 MeV.

average maximum amplification factor of energetic ion flux varies between ~4.5-7.5 in the energy range 0.112 - 4.75 MeV (LEMS30 detector of EPAM instrument on the ACE spacecraft), and between ~3.5-5.5 in the energy range 0.066 - 4.75 MeV (LEMS120) with the largest amplification factor occurring at the highest energies. The latter range of maximum amplification factors agree best with the analytical results. The analytical solution also predicts a systematic shift in the position of the maximum amplification factor. It varies from ~0.05-0.1 AU from low to high particle energies downstream of the injection point that does not appear to be present in the observations of current sheets in Figure 2, and in Figures 10 and 11 of [9]. However, the shift in the amplification factor is visible in energetic ion observations of SMFR acceleration behind an interplanetary shock from the Ulysses spacecraft at ~ 5 AU [5], and in ACR observations from the Voyager 2 spacecraft behind the solar wind termination shock [3, 7]. This can be explained by the fact that the typical size of SMFRs beyond 1 AU is larger. It enables particle acceleration and the associated peak formation in the particle flux to occur over a wider range of particle energies, thus making it easier to detect the shift in the amplification factor. Even so, the shift is quite clear in the new data analysis results at 1 AU shown

Figure 1(c). This became possible (i) because SMFRs was the direct focus of the analysis instead of the current sheets that separate SMFRs in [9], and (ii) because improved statistics was achieved by analyzing and averaging energetic ion fluxes for ~10 times more SMFR events than in [9] that employed a database of randomly chosen reconnecting current sheets.

In Figure 3, right panel, we present the corresponding accelerated energetic proton spectra from our analytical solution for 2nd order Fermi acceleration at the particle source (solid black curve), and at increasing distances further downstream of the injection location. The spectra are normalized so that the distribution function at the particle source has a value of one at the lowest momentum shown ($p/p_0 = 1.5$, where p_0 is the injection momentum specified to be at a suprathermal proton kinetic energy of $T \approx 1$ keV). At the particle source location the accelerated spectrum is close to a power law, being slightly softer than $f(p) \propto p^{-5}$ (in terms of differential intensity (particle flux) with respect to kinetic energy T it is somewhat harder than $j_T(T) \propto T^{-1.5}$) except at the lowest momenta where the spectrum steepens somewhat. Inspection of the spectral evolution with increasing distance downstream of the particle source reveals that the spectra become progressively harder and more exponential so that spectra at low energies are considerably harder compared to high energies. If one would fit a power law to the exponential spectrum at 0.2 AU downstream of the injection location (dashed cyan curve), the spectrum would be approximately a $f(p) \propto p^{-4}$ ($j_T(T) \propto T^{-1}$) above ~100 keV ($p/p_0 > 10$). This basic trend of spectral hardening and increasing exponential nature of accelerated proton spectra produced by SMFRs with increasing distance inside the SMFR region is consistent with SMFR acceleration events at 1 AU reported by Adhikari et al. [6], e.g.. The variation in the power-law index for differential intensity through the SMFR region from ~-1.5 to ~-1 for particle energies ~100 keV < T < 1 MeV in the second event discussed by Adhikari et al. is close to the result reported here. Similar hardening trends in the energetic particle spectra through a SMFR at ~5 AU was detected in Ulysses data and beyond the heliospheric termination shock in Voyager 2 ACR data [5, 7].

We conclude that one can potentially reproduce the observed flux amplification of energetic ions as a function of particle energy and the evolution of the accelerated spectra through SMFR regions at 1 AU by focusing solely on 2nd order Fermi SMFR acceleration of energetic ions in response to statistical fluctuations (variance) in the compression and the parallel shear flow in SMFRs, and we found that this can be accomplished by specifying reasonable SMFR parameters in the acceleration expressions (for more detail, see [8]). Based on the SMFR parameters that we used we found that stochastic acceleration by the variance in the parallel reconnection electric field is the dominant 2nd order Fermi acceleration mechanism. Unfortunately, we were unable to model particle acceleration for this mechanism using solution (8) because the analytical solution only holds for D_0^I being independent of particle speed. 2nd order Fermi acceleration involving the variance in the SMFR parallel shear flow was the second most efficient, while 2nd order Fermi acceleration due to the variance in SMFR compression was the least efficient. However, due to our limited observational knowledge of the SMFR parameters that enter into the acceleration expressions, and because of limitations of the analytical solutions, it is difficult to draw definitive conclusions about the ranking of the different 2nd order Fermi acceleration mechanisms associated with the variance in SMFR fields. Further progress requires intensifying data analysis of SMFR acceleration events, while at the same time increasing the sophistication of the solutions.

5.2 1st order Fermi acceleration by SMFRs

Consider Figure 4 where we display analytical solution (8) in the limit where 1st order Fermi acceleration of energetic ions in response to the mean compression rate of SMFRs in a SMFR region at 1 AU is assumed to be dominant acceleration mechanism. Inspection of the results in the left panel for the spatial variation in the amplification factor in the accelerated particle distribution downstream of the particle source position show that they are remarkably similar to the results in Figure 3 for 2nd order Fermi acceleration. In other words, with either 1st or 2nd order second Fermi SMFR acceleration the observed enhanced energetic ion flux in SMFR regions at 1 AU in Figure 2 can be reproduced

reasonably well. The SMFR parameters specified in the 1st order Fermi solution closely follow those used in the 2nd order Fermi solution, except for the characteristic cross section and length of SMFRs that were reduced by a factor of four. However, the reduced values fall within the range of possibility given the little that we know of the statistics of SMFR parameters in SMFR acceleration regions in the solar wind, thus accentuating the need for more detailed analysis of SMFR properties in SMFR acceleration regions.

As can be seen in Figure 4, right panel, similar to the results for 2nd order Fermi acceleration, the modeled accelerated spectra for 1st order Fermi acceleration are power laws at the particle source position (black curve), exhibiting the same rollover trend qualitatively at lower particle energies downstream of the injection point. Quantitatively, however, the spectral rollover trend at lower particle energies and overall increasing spectral hardening downstream of the injection location are notably stronger in the case of 1st order Fermi acceleration due to the cutoff in the downstream spectrum at the injection momentum. This illuminates a key difference between the 1st Fermi acceleration solution, where all the particles that arrive downstream of the particle source location have been systematically accelerated to momenta larger than the injection momentum to form the low-energy cutoff at the injection momentum, and the 2nd order Fermi solution, where particles arriving downstream

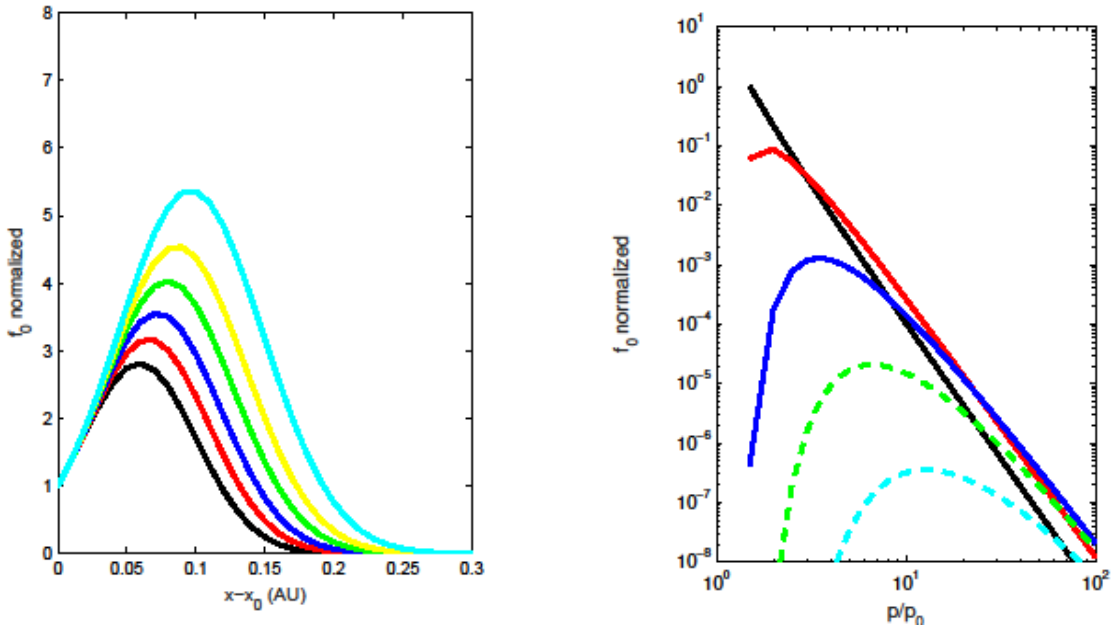

Figure 4. The 1D steady-state solution for energetic proton 1st order Fermi acceleration (mean SMFR compression acceleration) in a SMFR region in the vicinity of 1 AU based on equation (8). Left panel: The same format as Figure 3, left panel. Right panel: Same format as Figure 3, right panel.

experienced stochastic acceleration that lowers the probability for a low-energy cutoff at the injection momentum. This predicted difference in the spectral evolution for the two acceleration mechanisms downstream of the injection point might potentially be a helpful diagnostic for identifying the dominant operating SMFR acceleration mechanism in observations. Based on the evolution of the spectral power-law index through the SMFR region in SMFR acceleration event two of Adhikari et al. [6], the event with spectral power-law indices closest to our results, the less strong spectral hardening in the 2nd order Fermi acceleration case is closer to the observed hardening trend. However, but more SMFR acceleration events needs to be studied, and more realistic particle sources than a point source should be specified in the solution before conclusions can be drawn with confidence.

To the extent that we have achieved success in modeling SMFR acceleration characteristics results for 1st order Fermi but especially 2nd order Fermi acceleration near 1 AU for ions, this is partially due

to the term for particle escape from the SMFR region which ensured steepened accelerated particle spectra with more realistic slopes (see also [5, 6]). The particle escape term reflects the need for more sophisticated solutions that specify finite boundaries for the SMFR acceleration region and allow for multi-dimensional transport. However, the need for steeper accelerated spectra in the solution can partly be the result of modeling particle acceleration in the test particle limit. The considerable pressure in the accelerated test particle spectra indicates that the energy exchange between the particles and SMFRs should be modeled self-consistently, which would contribute also to steeper accelerated particle spectra [4, 11]. Simulations were also tried where both 1st and 2nd order Fermi SMFR acceleration of protons were combined. To reproduce the observational results in Figure 2, however, appears to require either 1st or 2nd order Fermi SMFR acceleration to be dominant, whereby the results were found to be very similar to those shown in Figures 3 and 4 for the separate acceleration mechanisms. A final note is that these solutions can also be used to model observations of energetic electron 1st and 2nd order Fermi acceleration by SMFRs as shown in Figure 2(c), a project that will be pursued in future research.

6. Justification and limitation of the steady-state solution

We find that both the time-dependent diffusive solution (6) and the telegrapher solution (2) produce identical results compared to the steady-state solution (8) for the spatial peaks in the distribution function of energetic particles accelerated by SMFRs after ~15 hours of acceleration in the case of 2nd order Fermi acceleration. Furthermore, the observations in Figure 2, and Figures 10 and 11 of [9], suggest that the average duration of a SMFR acceleration event is ~20-30 hours, implying that the radial extent of the average SMFR region is ~0.2-0.3 AU assuming that SMFRs are advected with the solar wind at a speed of ~ 400 km/s. Thus, the use of the steady-state solution to model observations at 1 AU, as done above, requires that a constant particle source be located at a radial distance not exceeding ~0.55-0.65 AU from the Sun. This constraint ensures that steady-state spatial peaks of a width of 0.2-0.3 AU will be advected past the observer at 1 AU. Such a steady state requires, however, that source particle injection into SMFR acceleration occurring beyond 0.55-0.65 AU is of negligible importance compared to injection from sources inside 0.55-0.65 AU. This is a reasonable zero'th order assumption given the effect of spherical expansion on reducing a background superthermal particle source with increasing heliocentric distance. The fact that a steady state requires particle transport from the source location over a radial distance interval of ~0.5 AU to reach Earth does raise the question of whether the assumption of spatially uniform coefficients in the analytical solution is sufficiently accurate and if a solution depending on heliocentric radial distance might be necessary. In conclusion, reproducing observations of energetic particles accelerated by SMFRs with steady-state planar analytical solutions should be seen as first reasonable step towards a more realistic time-dependent spherically-symmetric solution with transport coefficients that depends on radial distance and a particle source distributed throughout the SMFR region that will be attempted in future work.

7. Differences between the telegrapher and time-dependent diffusive solutions

The differences between the two types of time-dependent solutions, the telegrapher solution in equation (2) and the time-dependent diffusive solution in equation (6), can be illustrated best earlier during acceleration. We investigated these differences after ~3.1 hours of particle acceleration for 2nd order Fermi SMFR acceleration. Because of the causality condition $v_c\tau \geq d$ (see equation (4) and its discussion), the telegrapher solution imposes a cutoff on the maximum distance of diffusive particle propagation downstream of the particle point source position whereas in the time-dependent diffusive solution there is no cutoff. Consequently, plots of the spatial profiles of the distribution function of accelerated particles show spatial cutoffs downstream of the particle source position for the telegrapher solution, but only a gradual rollover for the time-dependent diffusive solution. We also notice that the spatial cutoffs shift increasingly further downstream of the particle source point with increasing particle energy in the telegrapher solution. This is consistent with the causality condition in the telegrapher solution which, simplified for 2nd order Fermi acceleration, reads

$$\frac{1}{3}v^2(t-t_0)^2 \geq (x-x_0)^2 + \frac{\kappa_0^I}{D_0^I}\left[\ln\left(\frac{p}{p_0}\right)\right]^2 \quad (11)$$

The condition indicates that faster propagating leading diffusive (nearly-isotropic) particle pulses at higher energies can propagate further downstream in a given time interval before cutoff ensues.

We also compared the evolution of the accelerated energetic particle spectra with increasing distance downstream of the particle source position inside the SMFR region for the telegrapher solution with the time-dependent diffusive solution after ~3.1 hours of acceleration. The results reveal that the telegrapher solution imposes momentum cutoffs in the spectra at lower particle energies whereas the diffusive solution exhibits a gradual spectral rollover without a cutoff at lower particle energies. In the telegrapher solution the low momentum spectral cutoffs occur at progressively higher particle momenta with increasing distance downstream of the particle source position as predicted by causality condition (11) (only the faster propagating leading diffusive particle pulses can reach the observer at larger distances downstream in a given time interval). At later times in the acceleration process the spatial and momentum cutoffs disappear from the displayed solutions (e.g., Figure 3) because they shift outside the spatial and momentum intervals of interest.

8. Summary

To facilitate modeling with analytical solutions, we presented a simplified 1D version of a new telegrapher-type Parker transport equation for the acceleration of energetic particles by contracting and reconnecting small-scale magnetic flux ropes (SMFRs) in the large-scale solar wind [8]. This equation was derived recently from the existing underlying focused transport equation [11]. It enabled new time-dependent solutions of the telegrapher Parker transport equation and of the time-dependent diffusive Parker transport equation in which the telegrapher term was neglected. By taking a late time asymptotic of the latter solution, a steady-state analytical solution was found. All these solutions unified all SMFR acceleration mechanisms present in the transport focused transport equation. An interesting feature of the telegrapher solution [8] is that SMFR acceleration by the parallel reconnection electric field of the mixed spatial and momentum derivative transport term [1] is constrained by and requires the presence of 2nd order Fermi SMFR acceleration. In other words, a complete description of acceleration by the parallel electric field requires that the 2nd order Fermi acceleration component of the acceleration by this electric field also be taken into account.

We explored the potential of the steady-state solution in reproducing energetic proton flux enhancements and spectral evolution between ~50 keV-5 MeV in dynamic SMFR regions near large-scale reconnecting current sheets or within magnetic cavities formed by such current sheets in the solar wind near Earth orbit. The results showed that 2nd order Fermi SMFR acceleration involving the variance in SMFR compression and incompressible parallel shear flow, and 1st order SMFR Fermi acceleration due to mean SMFR compression are both workable options in reproducing observed flux amplification factors when using reasonable SMFR parameters. The latter confirmed previous modeling efforts that emphasized 1st order Fermi acceleration [5, 6]. However, our solutions predicted substantial quantitative differences in the spatial evolution of the accelerated spectra through the SMFR region when 1st order Fermi acceleration was compared to 2nd order Fermi acceleration. We found downstream of the particle source that the 1st order Fermi acceleration spectrum cut off at the particle injection momentum at low energies, resulting in spectra that hardened and rolled over strongly at low energies. This is a direct consequence of the systematic nature of 1st order Fermi acceleration. On contrast, spectral hardening and rollover in the case of 2nd order Fermi acceleration was more modest, because there was no cutoff in the spectrum downstream at the injection momentum when acceleration was stochastic. We proposed that this difference in the spatial evolution of energetic particle spectra through SMFR regions might provide a diagnostic to distinguish between 1st and 2nd order Fermi SMFR acceleration in observations.

It was argued that a steady-state solution can be justified for modeling observations of SMFR acceleration at 1 AU as long as a constant particle source is specified not further from the Sun than ~0.55-0.65 AU. That provides enough time (~15 hours) for the accelerated particles to produce steady-

state spatial peaks before these peaks reach the observer at 1 AU. Finally, the results best illustrated differences in the telegrapher and time-dependent diffusive solutions during early acceleration times when the telegrapher solution exhibited spatial and momentum cutoffs in the accelerated particle distribution. At later times in the acceleration process the spatial and momentum cutoffs disappeared as they shift outside the spatial and momentum intervals of interest.

Acknowledgments
We thank J. Zheng, Q. Hu and Y. Chen for providing the SMFR ACE database (http://fluxrope.info) for our studies. The ACE EPAM LEMS120 data are from the CDAweb at http://cdaweb.gsfc.nasa.gov thanks to Dr. R. Gold of JHU/APL). J. A. le Roux acknowledge support from NASA Grants NNX15AI65G, 80NSSC19K027, NSF-DOE grant PHY-1707247, and NSF-EPSCoR RII-Track-1 Cooperative Agreement OIA-1655280. G. M. Webb was partially supported by NASA grant 80NSSC19K0075, and O. V. Khabarova by RFBR grants 18-52-06002 and 19-02-00957.

References
[1] Zank G P, le Roux J A, Webb G M, Dosch A and Khabarova O V 2014 *Astrophys. J.* **797** 28
[2] le Roux J A, Zank G P, Webb G M and Khabarova O V 2015 *Astrophys. J.* **801** 112
[3] Zank G P, Hunana P, Mostafavi P, le Roux J A, Li G, Webb G M, Khabarova, O V, Cummings A C, Stone E C, Decker R A 2015 *Astrophys. J.* **814** 137
[4] le Roux J A , Zank G P, Webb G M and Khabarova O V 2016 *Astrophys. J*. **827** 47
[5] Zhao L -L, Zank G P, Khabarova O V, Du S, Chen Y, Adhikari L and Hu Q 2018 *Astrophys. J. Lett*. **864**, L34
[6] Adhikari L, Khabarova O V, Zank G P, Zhao L-L 2019 *Astrophys. J*. **873** 72
[7] Zhao L -L, Zank G P, Hu Q, , Chen Y, Adhikari L, le Roux J A, Cummings A C, Stone E C and Burlaga L F 2019 *Astrophys. J.* **886** 144
[8] le Roux J A, Webb G M, Khabarova O V, Zhao L-L, Adhikari L 2019 *Astrophys. J*. **887** 77
[9] Khabarova O V and Zank G P 2017 *Astrophys. J*. **843** 4
[10] Che H and Zank G P 2020 *Astrophys. J.* **889** 11
[11] le Roux J A, Zank G P and Khabarova O V 2018 *Astrophys. J*. **864** 158
[12] Khabarova O V, Zank, G P, Li G, Malandraki O E , le Roux J A and Webb G M 2016 *Astrophys. J*. **827** 122.
[13] Chen Y, Hu Q and le Roux J A 2019 *Astrophys. J*. **881** 58